J. Fluid Mech. (2005), vol. 536, pp. 321–345. © 2005 Cambridge University Press
doi:10.1017/S0022112005004945 Printed in the United Kingdom

Compressible flow of liquid in a standing wave tube

By YOUNGSHIK SHIN[1†], JAEWON CHUNG[1‡],
NICK KLADIAS[2], ELIAS PANIDES[2],
GERALD A. DOMOTO[2] AND COSTAS P. GRIGOROPOULOS[1¶]

[1]Department of Mechanical Engineering, University of California, Berkeley, CA 94720-1740, USA
[2]Xerox Wilson Center for Research and Technology, 141 Webber Avenue, Sleepy Hollow,
NY 10591, USA

(Received 19 December 2003 and in revised form 21 February 2005)

Particle image velocimetry (PIV) has been applied to the study of acoustic flow of liquid in a standing wave tube. Even though liquid compressibility is very small, the liquid must be treated as compressible in this case. With the finite compressibility of liquid in mind, a series of different standing wave modes can be formed by pressure waves emanated at specific driving frequencies from a bimorph piezo disk at the end of the tube. In this paper, the first three natural standing wave modes were visualized using 1 μm diameter fluorescent microspheres seeded in the liquid. The variation of the flow field in the acoustic boundary layer near the wall was measured using PIV. Water was first used as a working fluid. Experiments were then carried out with a glycerol–water mixture (50 %–50 % by volume) to examine the effect of viscosity change on the wave propagation and flow structure inside the tube. The experimental results are compared with theoretical model predictions.

1. Introduction

The acoustic flow field in standing wave tubes has been studied for quite a long time theoretically, but experimental measurements have been scarce and very limited. Several different techniques (i.e. laser Doppler anemometry (LDA), probe microphones, Rayleigh, etc.) are available for measuring acoustic parameters in liquids and gases. Most of these, however, are point-measuring techniques. In contrast, particle image velocimetry (PIV) can provide detailed flow structure over the entire flow field (Adrian 1991). However, to the authors' knowledge, there is no published work on the flow field measurement of standing waves in liquid, as the acoustically driven boundary layer thickness is small for several kHz of driving frequencies.

The only substantial work to measure acoustic oscillatory motion using PIV has been carried out by Hann & Greated (1997 (*a*,*b*,*c*)). Hann & Greated set up the experiment to measure the oscillatory displacement amplitude of air in a tube of square cross-section wherein a standing wave was formed. A thin sheet of light produced by a 2 W argon-ion laser was used to illuminate the tube and the flow was visualized by the introduction of smoke particles just before the flow images were

---

† Present address: DA Research Center, Samsung Electronics Co., Ltd., Suwon, Korea
‡ Present address: Department of Mechanical Engineering, Korea University, Seoul, Korea
¶ Author to whom correspondence should be addressed: cgrigoro@me.berkeley.edu

taken. Rather than using conventional PIV technique, the particles were continuously exposed over several oscillation periods and thus particle streaks as long as several hundred micrometres were formed. The particle velocity was estimated by analysing these particle streaks.

Due to the small compressibility of liquid, oscillatory displacement amplitude in liquid is smaller than that in air, which makes accurate experimental measurement challenging. Vignola, Berthelot & Jarzynski (1990) measured the acoustic particle displacement of standing waves generated in a water-filled tube using the Doppler shift of laser light scattered from colloidal microparticles oscillating under the action of an acoustic field. This was a point measurement.

In this paper, the flow structure inside a standing wave tube filled with liquid is studied experimentally. Since the acoustic wavelength comparable to the total length of the tube is greater than the cross-sectional dimension, the wave propagation through the liquid medium inside the standing wave tube can be approximated as one-dimensional. That is to say, once the piezo disk is actuated at a natural frequency, the liquid medium inside the tube can be thought to behave as an elastic solid bar whose one (the closed, in contact with the piezo) end is subject to a periodic velocity boundary condition, while the other (open) end is free. The liquid medium undergoes periodic compression and expansion in response to the driving frequency. The velocity profile across the tube is nearly flat, except in the very thin viscous region near the wall. At the solid boundary, the fluid has to satisfy the no-slip condition, which results in an acoustic boundary layer.

To study the flow structure inside the standing wave tube, experiments were carried out in three different ways: (i) visualization of standing waves and overall shape measurement in the core region, (ii) bandwidth characteristics (the displacement amplitude is acquired as a function of driving frequency), and (iii) variation of velocity vector field in the acoustic boundary layer adjacent to the wall during a cycle of operation using the PIV technique. The same set of experiments was carried out with a glycerol–water mixture (50 %–50 % by volume) to examine the effect of viscosity on the wave propagation and flow structure inside the standing wave tube. These experimental results are also compared with theoretical predictions. This work provides an understanding of the fundamentals of acoustic wave interactions in slightly compressible liquids within structures that are representative of piezoelectrically driven fluidic devices including inkjet printheads.

2. Experimental setup and technique

2.1. *Fabrication of the standing wave tube*

The standing wave tube was made by gluing a bimorph piezo disk (diameter: 6.4 mm) to the end of a square-cross-sectional Pyrex tube (inner dimension: 3 mm × 3 mm, length: 31 mm, wall thickness: 0.5 mm) with epoxy, as figure 1 shows. Table 1 summarizes the material properties of Pyrex. The bimorph piezo disk bows in and out like a drumhead when actuated with a voltage signal and the amplitude of displacement is thus proportional to the voltage signal supplied.

The tube was filled with liquid seeded by 1 μm fluorescent microspheres (≈0.01 % by volume) using long flexible tubing connected to the syringe. The filling was carried out very slowly and carefully from the closed end to the open end to prevent any bubbles from being trapped inside the tube. Because of the small inner dimension (3 mm × 3 mm) of the standing wave tube, surface tension is sufficiently strong to hold the liquid meniscus at the open end and prevent collapse after filling is completed.

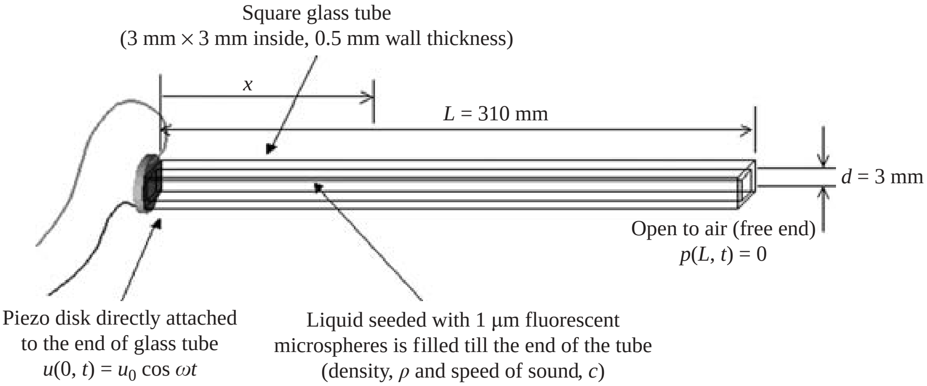

FIGURE 1. Configuration of the standing wave tube. A 6.4 mm diameter piezo disk is glued to one end of the tube with square cross-section and the other end is open to the air.

	Pyrex tube		PIV particles
Manufacturer	VitroCom. Inc.	Manufacturer	Molecular Probes. Inc.
Material	Borosilicate glass	Material	Polystyrene (carboxylate-modified) microspheres
Density	$\approx$2000 kg m^3	Density	1055 kg m^{-3}
Elastic modulus	$\approx 6 \times 10^{10}$ Pa	Size	1 μm
Poisson's ratio	$\approx$0.2	Compressibility	$\approx 0.46 \times 10^{-9}$ Pa^{-1}
Refractive Index	1.474 at 589 nm	Volume fraction	$\approx$0.01 %

TABLE 1. Material properties of Pyrex tube and PIV particles.

When the piezo disk is driven with a sinusoidal voltage signal (±160 V), plane acoustic waves are launched and propagate along the tube. These are reflected backwards at the interface of the open end. By driving the piezo disk at natural frequencies, a series of standing waves (e.g. first mode, second mode, third mode, etc.) can be excited inside the tube, as figure 2 shows. In this experiment, the first three natural modes of standing waves were visualized and the variation of the velocity field near the wall was measured using PIV for two different cases: (i) standing wave tube filled with water and (ii) standing wave tube filled with glycerol-water mixture (50 %–50 % by volume).

Seed particles in water could potentially affect the propagation of pressure waves along the standing wave tube. However, the density of seed particles is nearly the same as that of water and furthermore the concentration of seed particles used in this experiment is low (∼0.01 % by volume). Consequently, the effect of seed particles can be neglected in this regard.

In our initial tests of this standing wave tube, the natural frequency decreased with time. This was caused by microbubbles released from the piezo surface, glass wall, and the fluid itself. For example, the addition of bubbles as small as 0.01 % in volume can transform the simple medium into a highly dispersive and nonlinear one and the effective sound speed of the host medium decreases more than 40 % (Wilson 2002). Degassing in a vacuum chamber after filling liquid in the standing wave tube diminished the generation of microbubbles.

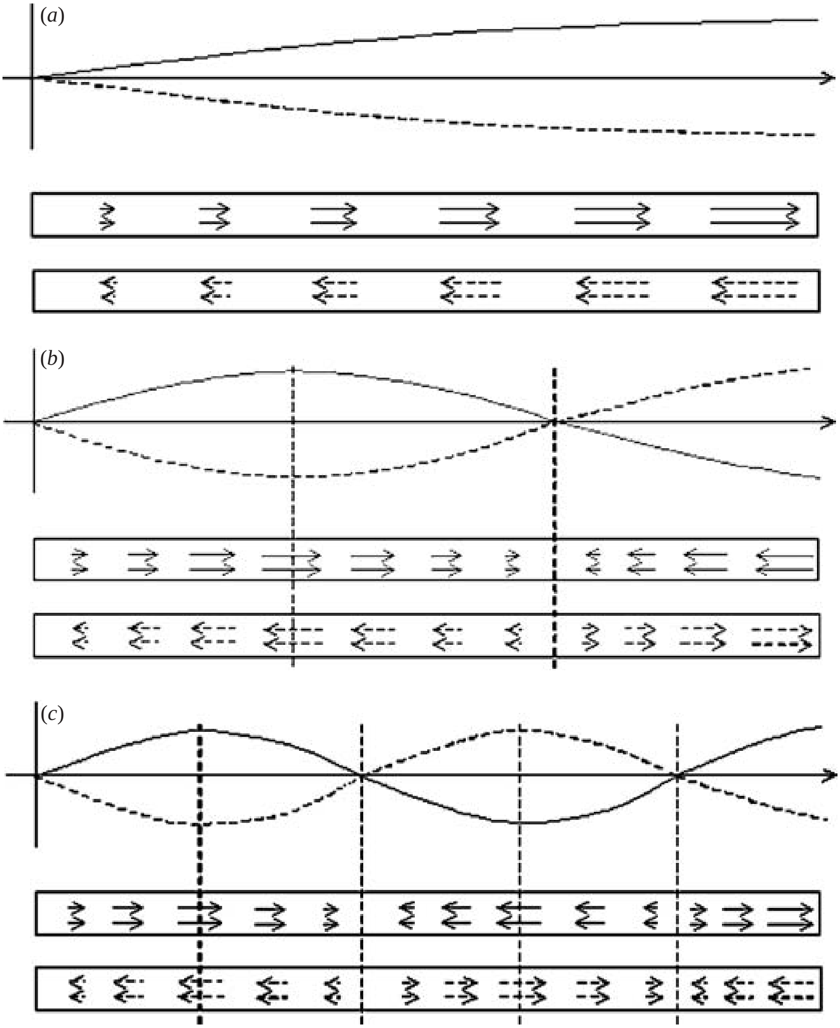

Figure 2. The first three natural modes of standing waves in the tube for the driven (left-hand end) and free end (right) conditions: (*a*) first natural mode, (*b*) second natural mode, (*c*) third natural mode.

It is noted that the effective speed of sound along the tube is significantly lower than that in unbounded liquid. This is because the Pyrex wall exhibits certain compliance that reduces the acoustic pressure in the liquid, resulting in significantly lower effective bulk modulus and speed of sound than what is observed in a liquid of infinite extent.

2.2. *Visualization of standing waves in the tube*

After filling with seeded liquid and degassing in the vacuum chamber, the fixture was mounted horizontally on a three-dimensional translation stage adjusting the position of the fixture within 10 μm spatial resolution as shown in figure 3. This three-dimensional translation stage was mounted on a long-distance, computer-controlled translation stage that travels over the total distance of the tube from end to end. The bimorph piezo disk was driven by ±160 V sinusoidal voltage signal from the function generator and voltage amplifier.

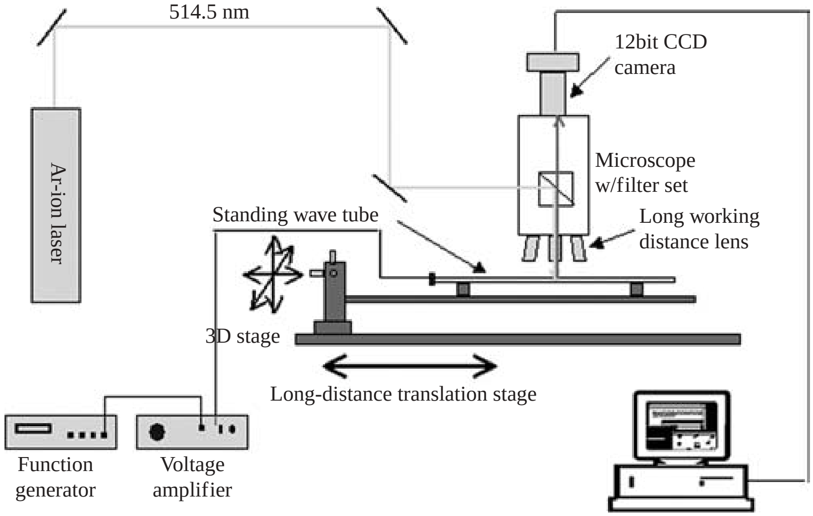

FIGURE 3. Experimental setup to visualize the standing waves in the tube. The fixture is mounted on the long-distance translation stage that is controlled by a computer. An argon-ion laser (continuous) is used for illumination of the flow field and the piezo disk is driven by ±160 V sinusoidal voltage signal from the function generator and amplifier. A long enough exposure time is provided to the highly sensitive 12 bit CCD camera to capture the streak images of the fluorescent seed particles that absorb green light and emit red light. An appropriate filter set including a dichroic mirror and band-pass filter is used inside the microscope. A 50 × long working distance objective lens is used for imaging.

The flow field inside the tube was illuminated volumetrically using a continuous argon-ion laser (wavelength: 514.5 nm). Once the piezo disk is driven, fluid particles oscillate along the tube with their displacement reaching maximum amplitude at the time instant of the standing wave formation. By allowing long enough exposure time (i.e. several times greater than the period of oscillation), streak lines of the oscillating particles could be observed. To determine the natural frequencies, the driving frequency was varied slowly while the region near the open end that is anticipated to be riding an antinode was monitored. This is where the longest streak lines are observed. To visualize the overall shape of the standing waves, images were taken marching along the tube towards the closed end. The focal plane was located at a distance of about 200 μm below the top glass wall/liquid interface. Because the displacement of particles is mostly uniform across the square tube except in the very thin region (on the order of several tens of microns) near the wall, the location of the focal plane was not important provided it was outside the acoustic boundary layer. In this way, a series of images containing streak lines at several different positions along the standing wave tube were obtained (figure 4) and compared with a reticle image that was taken with the same recording optics to measure the length of each of these streak lines using image analysis software.

2.3. *Velocity field measurement near the wall using PIV*

In addition to the above experiment on the visualization of the overall shape of standing waves, a PIV experiment was carried out to measure the temporal variation of the velocity field near the wall in the acoustic boundary layer (see figure 5). The basic idea of the PIV experiment is that positions of flow-tracing particles are recorded at two known times by illuminating the particles using a pulsed light source.

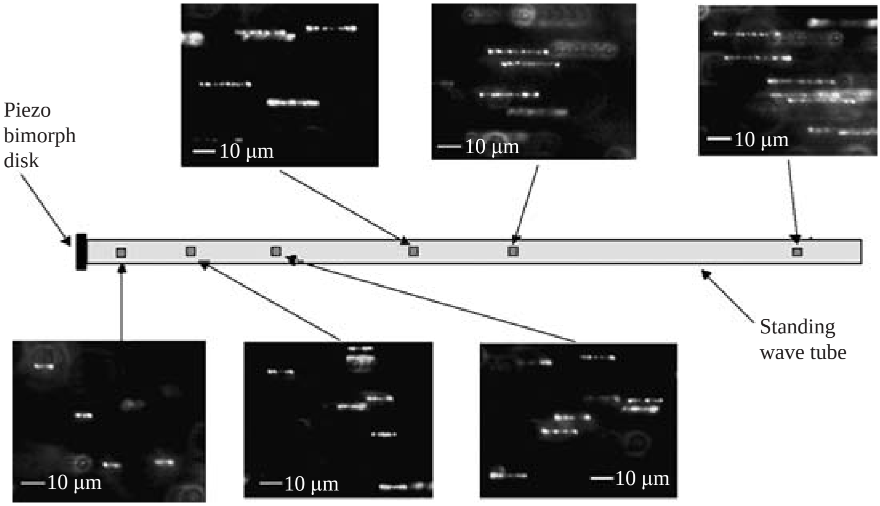

FIGURE 4. Visualization of standing waves in the tube. Some images depicting the displacement amplitude at several different positions along the tube are shown for the first mode.

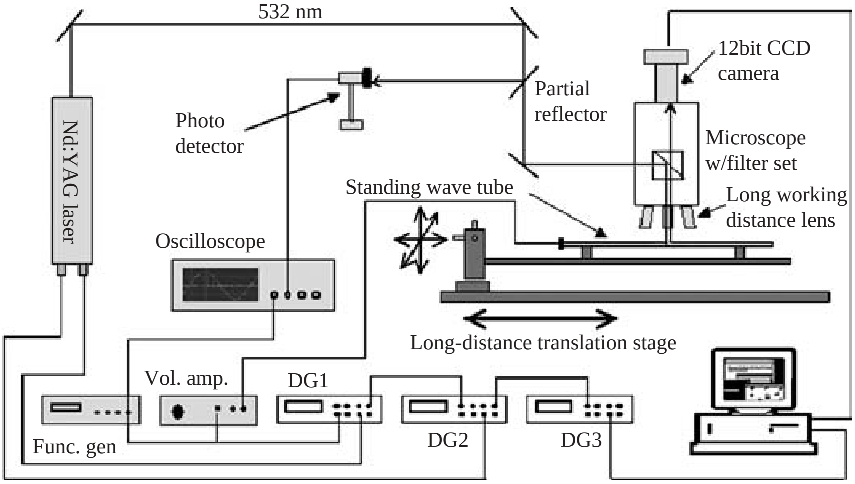

FIGURE 5. Experimental setup to acquire flow images at the right timing. An Nd:YAG laser (nanosecond pulsed) is used for illumination. Since the two laser firings, camera triggering, and piezo actuation all need to be synchronized, three delay generators are connected to each other as well as to the relevant devices. To check the temporal location of the laser pulse in the sinusoidal voltage signal for every pair of flow images, a tiny portion of laser light is extracted by the partial reflector, detected with the photodetector and recorded in the oscilloscope.

The displacement fields are then estimated statistically by correlating particle image pairs (Meinhart, Wereley & Santiago 1999). When the standing wave was formed inside the tube, pairs of particle images with a known temporal spacing Δt, were obtained at several different time instants. All these images were taken inside a small region of about 190 μm × 150 μm near the wall, at a distance of 2 cm from the open end. A Nd:YAG laser (10 mJ, 532 nm) with 7 ns pulse duration was used to excite the fluorescent particles whose decay time is about 10 ns. The fluorescent images are then recorded using a cooled interline transfer, 1280 × 1024 pixel, 12 bit CCD camera

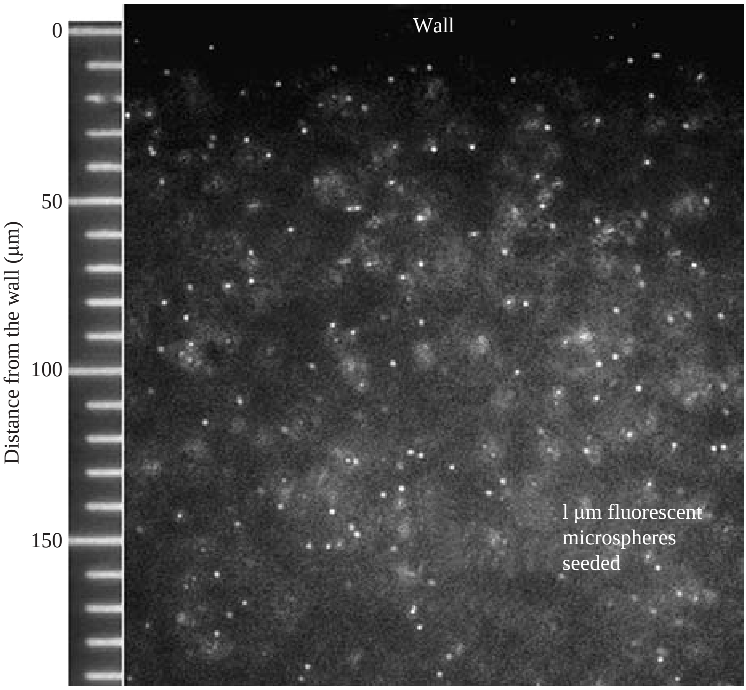

FIGURE 6. Flow image for velocity vector calculation. The image is taken at a location near the wall, 2 cm from the open end (anti-node) and the focal plane of the optical system is located about 200 μm below the top wall/liquid interface. The exposure time for all of these images is about 10 ns which is imposed by the pulse width of the Nd:YAG laser.

(SensiCam, Cooke Corp.) that is capable of acquiring back-to-back images separated by a time interval as short as 200 ns.

Firing two laser pulses at the right timing is critical in this experiment. Furthermore, it is required to know where these two pulses are located in the driving sinusoidal voltage signal. To achieve this, a partial reflector, photo detector, oscilloscope, and three delay generators were used. These were connected to each other via a function generator and computer. Some of the details about timing control will be discussed in § 2.8. Figure 6 shows one example of flow images taken in this way. After flow images are taken, the displacement vectors are then estimated statistically by correlating the flow image pairs. The velocity vector field can be acquired by dividing displacement vectors by the temporal spacing between the two images, Δt.

2.4. *Seed particles*

The basic assumption for validity of the PIV experiment is that the seed particles follow the motion of fluid faithfully. There are conflicting demands on the seed particles, with respect to the flow-tracking capability and the necessary amount of scattered light for detection. If the particle size increases, the amount of scattered light increases, which is helpful, but it also increases the slip of particles versus fluid flow. If the particle size decreases, the ability of particles to accurately follow the flow increases, but the error due to Brownian motion can also increase. Therefore, a compromise between reducing the particle size (to improve flow tracking) and increasing the particle size (to improve light scattering) is necessary (Melling 1997).

In this experiment, polystyrene particles with diameters of 1 μm and specific gravity, $\rho = 1.055$ were used. These particles are tagged with fluorescent dye that absorbs light from a frequency-doubled Nd:YAG laser ($\lambda = 532$ nm) or argon-ion laser ($\lambda = 514.5$ nm), with a peak excitation wavelength of $\lambda_{abs} = 535$ nm and a peak emission wavelength of $\lambda_{emit} = 575$ nm. To cut the excitation light and sense the emission light only, a suitable bandpass filter and dichroic mirror were used.

2.5. *Error analysis*

As mentioned in § 2.4, using either big or small particles can cause errors. Several studies on the flow tracking capabilities of seed particles for application in PIV studies have been published in the past. Hjelmfelt & Mockros (1966) examined the behaviour of particles in a turbulent flow field. Another theoretical study can be found in Melling (1997), who investigated the response of particles downstream of an oblique shock.

(i) Error due to slip: Here, instead of doing a rigorous analysis on the accuracy of the measurement, the error due to the slip of particles is estimated approximately by assuming Stokes' drag as follows. The difference between the fluid and particle velocities can be written by

$$|\boldsymbol{u} - \boldsymbol{v}| = \frac{\rho_p d_p^2 |\dot{v}|}{18 \rho_f \nu_f} \tag{2.1}$$

where $\boldsymbol{u}$ is the fluid velocity, $\boldsymbol{v}$ is the particle velocity, ρ_p is the particle density, d_p is the diameter of the particle, $\dot{v}$ is the total time derivative of the particle velocity, ρ_f is the density of fluid, and ν_f is the kinematic viscosity of the fluid. From the maximum measured velocity of about $0.15\,\mathrm{m\,s^{-1}}$ (in the case of the third natural mode driven at $f = 3800$ Hz) and its sinusoidal dependence in time ($v = 0.15 \cos \omega t$), the maximum acceleration can be estimated by $|\dot{v}| = |-0.15\omega \sin \omega t| = 0.15(2\pi)(3800) = 3581.4\,\mathrm{m\,s^{-2}}$. For polystyrene particles in water, which have a specific gravity of $\rho_p/\rho_f = 1.055$, and taking the kinematic viscosity $\nu_f = 1.006 \times 10^{-6}\,\mathrm{m^2\,s^{-1}}$, it is inferred that the 1 μm diameter particle will slip a maximum of about $2.1 \times 10^{-4}\,\mathrm{m\,s^{-1}}$. For the maximum velocity of $0.15\,\mathrm{m\,s^{-1}}$, the maximum error due to slip is approximately 0.14 %. For polystyrene particles in glycerol–water mixture, the error is smaller since viscosity is higher than that of water.

(ii) Error due to Brownian motion: The error due to Brownian motion can be defined as the ratio of the random mean-square particle displacement associated with Brownian motion to the displacement associated with the standing wave motion following the procedure described in Santiago *et al.* (1998):

$$\varepsilon_B = \frac{\langle s^2 \rangle^{1/2}}{\Delta x} = \frac{1}{v}\sqrt{\frac{2D}{\Delta t}}, \tag{2.2}$$

where D is the Brownian diffusion coefficient, v is the characteristic velocity, and Δt is the temporal spacing between the two flow images. D can be estimated by the following relation which is often referred to as the Stokes–Einstein equation:

$$D = \frac{k_B T}{6\pi \nu_f r_p}, \tag{2.3}$$

where k_B is the Boltzmann constant, T is the absolute temperature, r_p is the radius of the seed particle. Using a diffusion coefficient D estimated from the above equation, a characteristic velocity of $v = 0.1\,\mathrm{m\,s^{-1}}$ and temporal spacing of $\Delta t = 27$ μs, the error due to Brownian motion of a 1 μm diameter particle is about 5 % and the aggregate error of particles can further be reduced. Therefore, the error due to Brownian motion is not significant in these experiments.

2.6. *Volumetric illumination*

In the PIV experiment, illumination is usually done by a sheet of light. In this case, however, the optical access is limited and the flow field domain of interest is in the microscopic scale. Therefore it is preferable to apply volumetric illumination on the entire fixture, as opposed to a two-dimensional light sheet. Only particles within the depth of focus can be visualized, thereby defining the so-called measurement plane.

The depth of focus was about 3 µm for the optical system used in this experimental setup. Basically, only the particles moving at and close to the focal plane yield a signal. Particles outside the focal plane create background noise that decreases the signal to noise ratio. For a fixed illumination depth (i.e. inner cross-sectional dimension of the tube), the level of background noise can be lowered by decreasing the concentration of seed particles (Meinhart, Wereley & Gray 2000). In this case, the inner dimension of the tube was relatively large (3 mm × 3 mm). Hence, a low volume concentration ($\sim$0.01 %) of seed particles had to be used, resulting in low spatial resolution in the PIV experiment since a lower concentration of seed particles requires the use of larger interrogation regions to obtain an adequate correlation signal. Also, for the given tube cross-sectional dimensions and seed particle concentration, the signal to noise ratio of the in-focus particle image decreases as the distance between focal plane and the tube wall increases. In other words, it is increasingly harder to distinguish the in-focus particles with enough contrast as the focal plane is moved deep into the liquid. For the particle concentration of 0.01 % by volume in this experiment, high enough signal to noise ratio could be achieved only in the region near the wall to a depth of about 500 µm.

2.7. *Imaging and recording*

Within 200 ns after the first frame taken by the interline transfer CCD camera, the image field is transferred to storage pixels, so that a second image can be recorded. The camera is cooled to $T = -11^{\circ}\mathrm{C}$ to minimize the readout noise so the weak fluorescent signal can be measured. A long-working-distance objective lens (NA. = 0.42, Magnification = 50 ×) was used to examine the flow in the core region of the tube under 500 µm thick the top wall.

2.8. *Timing control*

As mentioned in § 2.3, to locate the laser pulses and trigger the camera at the right timing, two laser firings, the camera triggering, and the actuation of the piezo disk at the end of the standing wave tube, need to be synchronized. A sinusoidal voltage signal (± 8 V) from a function generator was sent to the voltage amplifier where the amplitude was increased by a factor of 20 (± 160 V) and then was used to drive the piezo disk. Also, the same sinusoidal signal from the function generator was sent to the first delay generator. The first delay generator triggers the second delay generator and the second delay generator triggers the third delay generator. The second delay generator was used for both triggering the camera and firing the first laser pulse and the third delay generator was used to trigger the second laser firing. As figure 7 shows, the camera opens for the first frame during the TTL signal from the second delay generator is on and opens itself again for the second frame, 200 ns after the first frame is closed. Basically, the pulse width of the laser light determines the exposure time of the flow image. To acquire a more consistent flow by eliminating the initial

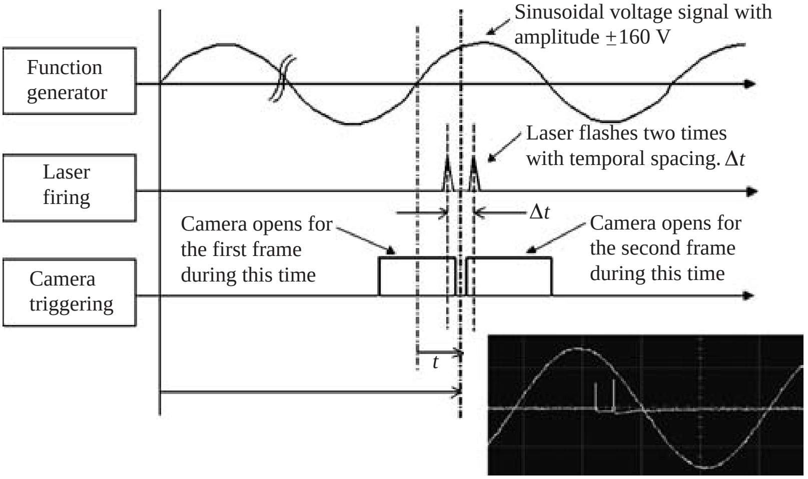

FIGURE 7. Timing control diagram. Sinusoidal voltage of ±160 V is provided to the bimorph piezo disk by the function generator and voltage amplifier. The function generator triggers the delay generator and the signal from the delay generator triggers the laser firing. The camera opens for the first frame when the TTL signal from the delay generator is on and opens again for the second frame 200 ns after the first frame is closed.

flow transients, the two laser pulses were fired during the 51st cycle after the first 50 periods.

To check all these timings, a partial reflector was placed in the laser beam path just before the microscope and a small portion of light was sampled and directed onto a photodetector connected to an oscilloscope. The sinusoidal driving signal from the function generator was also fed into the oscilloscope. Therefore, whenever flow image pairs were taken, the corresponding timing diagram was also acquired and the temporal location of the two laser pulses relative to the sinusoidal driving signal could be accurately identified.

2.9. *Vector processing*

The PIV images were analysed using standard cross-correlation methods. In order to achieve sufficiently large signal to noise ratio, the seed particle solution was diluted. To ensure a sufficiently high number of seed particles per interrogation window for generating high-quality data, 16.2 μm × 16.2 μm of the interrogation region and 3.2 μm × 2.4 μm of the cross-correlation offset were chosen. The results were averaged over several pieces of data acquired at the same phase. Based on the size and overlapping of the interrogation region, the velocity vector spacing was 7 μm × 10 μm, in the directions normal and parallel to the wall, respectively. Note that the spatial resolution (i.e. the velocity vector spacing) is determined by the size and offset of the interrogation region, which depend on the imaging system, the size and number density of particles.

3. Results and discussion: tube filled with water

The standing wave tube was filled with water and the measurements were carried out after degassing in the vacuum chamber. The overall shape of standing waves in the tube was visualized and bandwidth characteristic was measured. The velocity field

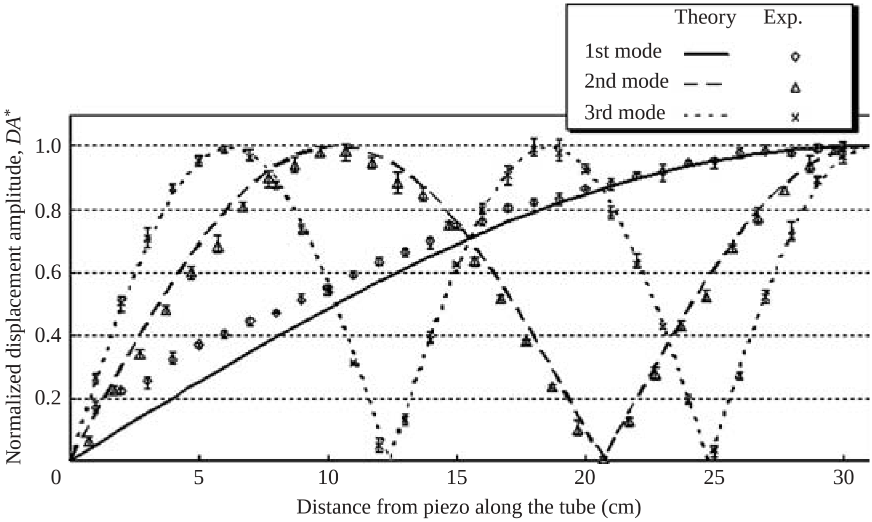

FIGURE 8. Normalized displacement amplitude, DA^* ($=DA/DA_{\max}$) at the first three natural modes of a standing wave inside the tube filled with water. The first natural mode was observed at 690 Hz and $DA_{\max}$ was 26 µm. The second natural mode was observed at 2330 Hz and $DA_{\max}$ was 15 µm, and the third natural mode was observed at 3800 Hz and $DA_{\max}$ was 16–17 µm. The detailed procedure for obtaining the theoretical curve is explained in § 3.4.1.

variation near the wall was measured using PIV and compared with theory for the first three natural modes.

3.1. *Overall shape of standing wave for the first three natural modes*

Figure 8 shows normalized displacement amplitudes, DA^* along the standing wave tube for the first three natural modes. DA^* is defined as the displacement amplitude, DA divided by the maximum displacement amplitude, $DA_{\max}$: (*a*) is the first natural mode observed at 690 Hz and $DA_{\max}$ is 26 µm, (*b*) is the second natural mode at 2330 Hz and $DA_{\max}$ is 15 µm, and (*c*) is the third natural mode at 3800 Hz and $DA_{\max}$ is 16–17 µm. The detailed procedure for obtaining the predicted curves is described in § 3.4.1. For all three cases, the left-hand closed end behaves as a nodal point and the right-hand open end as an antinode. For the second natural mode (the third harmonic), there is an additional node at 2/3 of the total length of the tube. For the third natural mode (the fifth harmonic), there are two more nodes at 2/5 and 4/5 of the total length of the tube.

From the observed natural frequencies of 690 Hz, 2330 Hz, and 3800 Hz for the first, second, and third modes respectively, the effective speed of sound can be estimated as 856 m s^{-1}, 963 m s^{-1}, and 942 m s^{-1}, which is significantly lower than in unbounded water (~1480 m s^{-1} at 20 °C). This reduction can also be calculated theoretically by solving the problem of wave propagation in a liquid-filled elastic tube (Lafleur & Shields 1995). As mentioned in § 2.1, this slower effective speed of sound is caused by the small, but finite elasticity of the tube wall material.

In figure 8, the displacement amplitude near the nodal point at the closed end (left-hand side) is very small (less than a micron) if the data are extrapolated to the origin for the second and third modes. However, the displacement amplitude of the first mode at the node is somewhat bigger than in the other two cases. This might be caused by the longer wavelength (~1.2 m) of the first mode. As the wavelength corresponding to the driving frequency increases, the fluid inside the tube has a greater

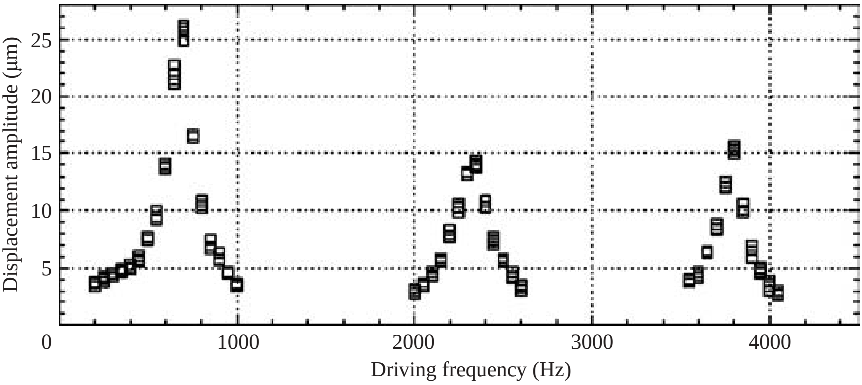

FIGURE 9. Bandwidth measurement for the first three natural modes (water).

tendency to move as a lumped mass. In the case of the first mode, the wavelength is four times longer than the tube length and some deviation from the natural frequency can result in the appearance of this behavior.

As figures 8(*b*) and 8(*c*) show, two antinodes are formed for the second natural mode and three for the third natural mode. The peak amplitudes are nearly the same in both these modes, implying that dissipation by absorption can be considered negligible.

3.2. *Bandwidth measurement*

In figure 9, the displacement amplitude versus driving frequency is shown. The lengths of streak lines were measured near the antinode (2 cm from the open end) while the driving frequency was varied in a certain range around the natural frequency. While the displacement amplitude was highest in the first mode, there was no substantial difference between the second and third modes. The FWHM (full width half maximum) was about the same, in the range of 200–250 Hz for all three cases.

The bandwidth measurement for the first mode at three different positions (11, 21, 29 cm from the piezo disk) is depicted in figure 10. The point at the distance of 11 cm from the piezo is the closest to the node among the three points picked; evidently the displacement amplitude is lowest there. Asymmetric bandwidth profiles are observed in the low-frequency region, due to reasons briefly mentioned in § 3.1. As the driving frequency decreases, the wavelength increases and becomes much greater than the total length of the tube. This augments the tendency of the liquid to behave as a lumped mass inside the tube and results in the collapse of all data at frequencies below ∼550 Hz. On the right-hand side the displacement amplitude is lowest at 11 cm and highest at 29 cm from the piezo. The FWHM is almost the same for all three positions at about 200 Hz.

Figure 11 shows the bandwidth measurement for the second mode at three different positions between node and antinode (25 cm, 27 cm, and 29 cm from piezo). In this second natural mode, the node is at around 21 cm and the antinode at 31 cm. No asymmetric bandwidth profiles were observed, while the FWHM was ∼250 Hz. The FWHM is almost the same for all the three positions, at ∼250 Hz.

Figure 12 shows the bandwidth measurement for the third mode at three different positions between node and antinode (27 cm, 28 cm, and 29 cm from the piezo). In this third natural mode, the node is at around 25 cm and the antinode is at 31 cm. The

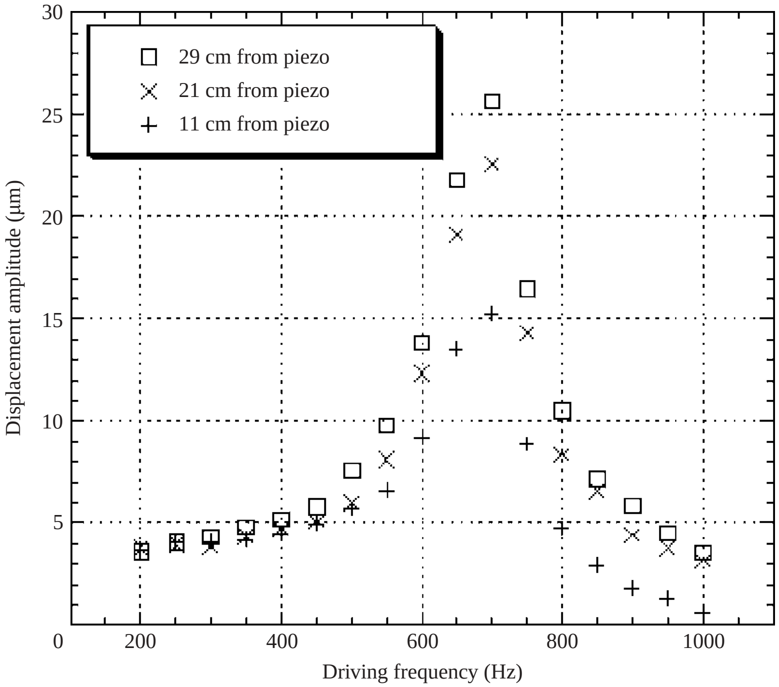

FIGURE 10. Bandwidth measurement for the first natural mode at three different positions of 11 cm, 21 cm, and 29 cm from the piezo disk (water).

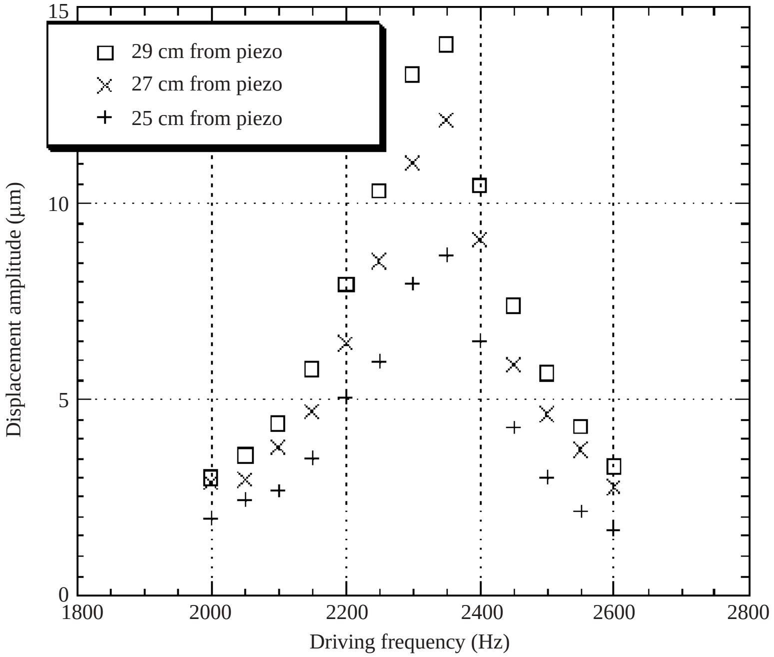

FIGURE 11. Bandwidth measurement for the second natural mode at three different positions of 25 cm, 27 cm, and 29 cm from the piezo disk (water).

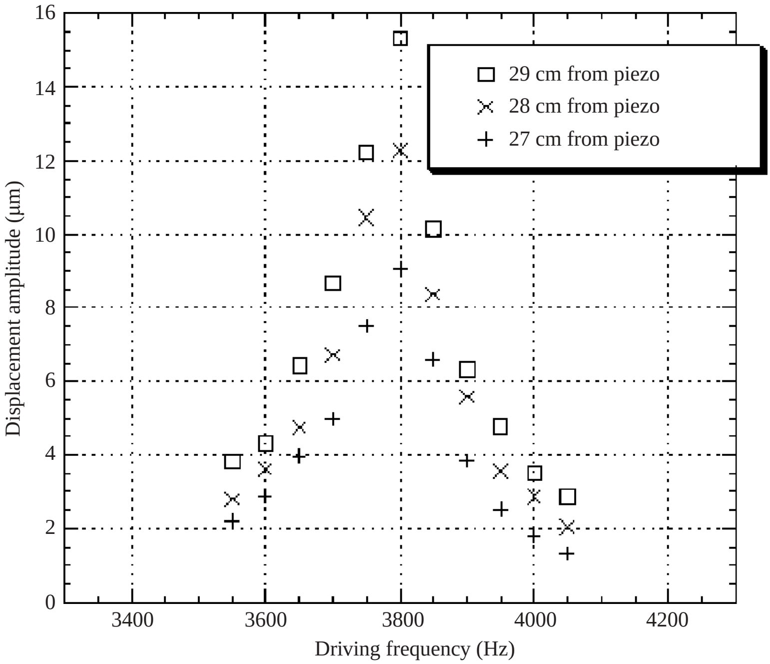

FIGURE 12. Bandwidth measurement for the third natural mode at three different positions of 27 cm, 28 cm, and 29 cm from the piezo disk (water).

displacement amplitude is lowest at 27 cm and highest at 29 cm since 27 cm is close to the node and 29 cm is close to the antinode. In this range of driving frequency, the wavelength is smaller than the total length of the tube and the data appear to be more symmetric with respect to the central frequency. The FWHM is almost the same for all three positions at ∼200 Hz.

3.3. *Flow field variation near the wall in the acoustic boundary layer*

For the two-dimensional 190 μm by 150 μm planar area near the wall and at a distance of about 2 cm from the open end (antinode), PIV images were taken during the 51st cycle, i.e. after the initial flow transients were damped out. The phenomenon was very repeatable. Cycle-to-cycle repeatability of the experiment was tested by comparing the results that were acquired at the same phase on two different cycles (51st and 52nd). Since the camera can acquire only two fast images at a time, this repeatability is critical in terms of the reliability of data.

Figures 13, 14 and 15 show that the velocity profile is nearly flat over most of the tube cross-section except in the very thin region near the wall. This seems to be reasonable, considering the one-dimensional nature of the wave propagating along the tube since the acoustic wavelength in the operating range of up to several kHz is much greater than the cross-sectional dimension of the tube. Therefore, the fluid inside the tube behaves like an elastic solid bar transmitting longitudinal pressure waves. The particles of this 'elastic solid bar' undergo compression and expansion in a periodic manner according to the driving frequency at the instant of the standing wave formation. The tube wall, however, is fixed and stationary. This is not true in a strict sense since the Pyrex wall is also an elastic medium where the wave propagates at a different speed, meaning that the wall also experiences expansion and compression along the tube. Nevertheless, the wall displacement amplitude can

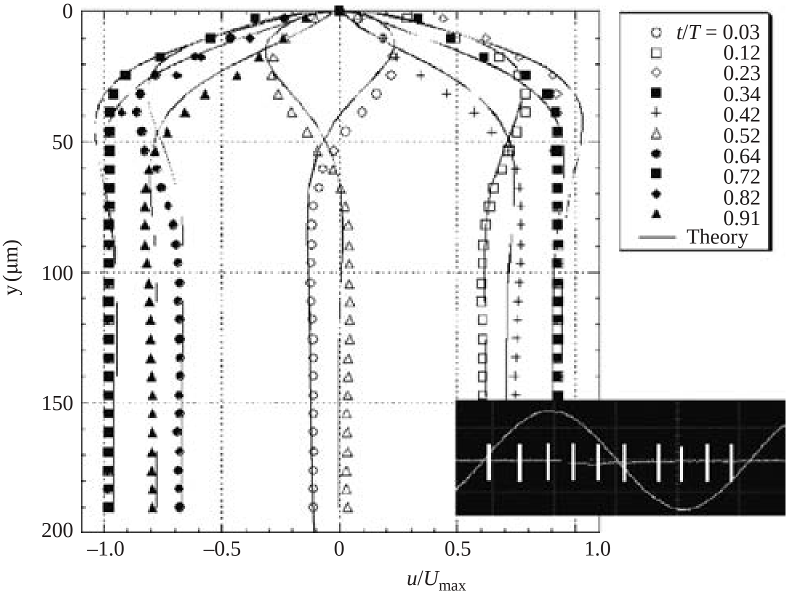

FIGURE 13. The variation of normalized velocity, $u/U_{\max}$ in the acoustic boundary layer near the wall during a cycle of operation for the first natural mode of standing wave. The maximum velocity in the core region during a cycle, $U_{\max}$ is about 45 mm s^{-1}. Each profile corresponds to the temporal location marked as a white bar in the sinusoidal voltage signal that is supplied to piezo disk. The detailed procedure for obtaining the theoretical curve is explained in § 3.4.3.

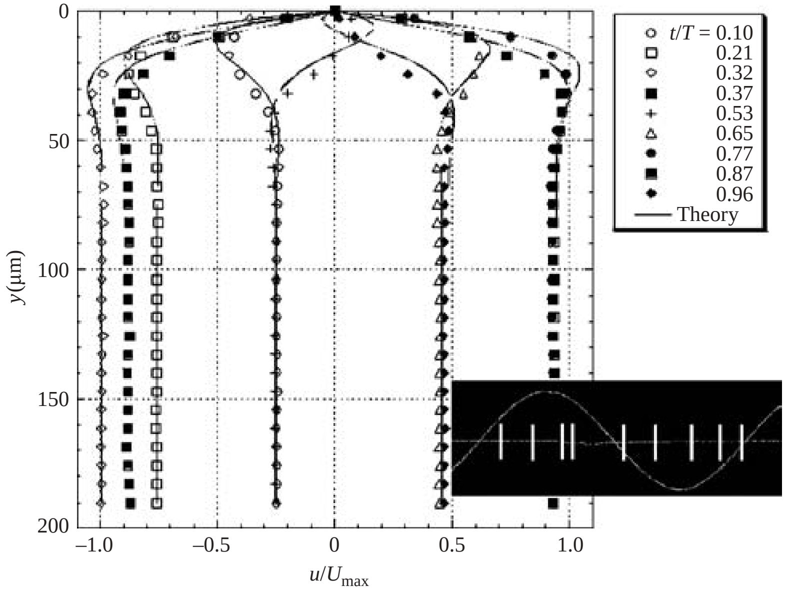

FIGURE 14. As figure 13 but for the second natural mode of standing wave. The maximum velocity in the core region during a cycle, $U_{\max}$ is about 100 mm s^{-1}.

be neglected since it is small compared to that of fluid particles. The fluid has to satisfy the no-slip condition at the wall boundary, which necessarily leads to the development of an acoustic boundary layer near the wall. The thickness of this

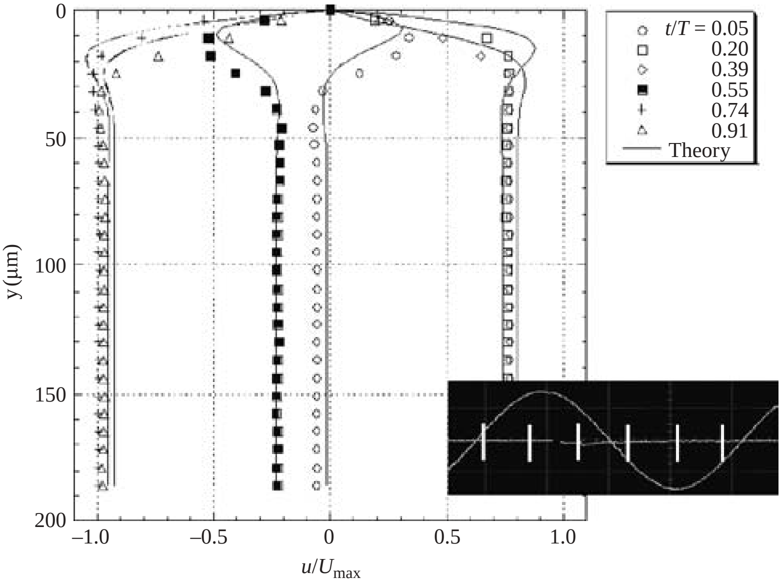

FIGURE 15. As figure 13 but for the third natural mode of standing wave. The maximum velocity in the core region during a cycle, $U_{\max}$ is about 150 mm s^{-1}.

acoustic boundary layer is on the order of several tens of microns for all three cases depicted in figures 13, 14, and 15 and decreases as the driving frequency increases (the thickness is inversely proportional to the square root of driving frequency, f). According to this observation, the two-dimensional measurement (or focal) plane was located at a distance of about 200 μm below the top wall/liquid interface, which is well beyond the acoustic boundary layer. If this measurement plane is located too close to the wall and inside the boundary layer, then the velocity in the core region will be underestimated and the flow structure will look different. Also, the flow at the measurement plane is nearly two-dimensional and the out-of-plane motion of fluid particles caused by acoustic streaming not significant (i.e. only the velocity component in the axial direction is substantial).

(i) First natural mode: The instantaneous velocity profiles obtained from PIV measurements for the first natural mode are shown in figure 13 for times $t/T = 0.03$, 0.12, 0.23, 0.34, 0.42, 0.52, 0.64, 0.72, 0.82, and 0.91. T is the period of the driving sinusoidal signal, which is 1449 μs in this case and t is the time elapsed from the zero phase of the driving sinusoidal signal. Since the driving sinusoidal signal and the timing of the PIV measurement, t, were not actively synchronized, the PIV measurements were carried out many times while measuring t with the oscilloscope to obtain the results in figure 13. Each velocity profile corresponds to a temporal location marked as a white bar in the driving sinusoidal voltage signal for the piezo. The velocity profile is obtained from the averaged velocity over 150 μm in the axial direction at a distance of 2 cm from the open end. This is acceptable because the velocity varies gradually over the entire tube length and can be considered nearly uniform over the short distance of 150 μm.

If the displacement of the piezo was exactly in phase with the driving sinusoidal voltage signal, the velocity in the core region would be close to maximum at $t/T = 0$. However, the measured velocity at $t/T = 0.03$ is nearly zero in the core region, which suggests the existence of a phase lag of about $\pi/2$ between the driving sinusoidal voltage signal and the response of the fluid. A detailed explanation on this observation will be given in § 3.4. In addition, at the velocity profile at $t/T = 0.03$ shows 'velocity reversal' near the wall. In other words, the fluid within about 50 µm from the wall is moving in the positive direction while the fluid in the core region is moving in the negative direction. At $t/T = 0.12$, all the velocity vectors are in the positive direction and their magnitudes larger. At $t/T = 0.23$, the velocity in the core region should be nearly zero if the piezo disk is displaced in phase with the driving signal. But the core velocity at $t/T = 0.23$ is around the maximum, which shows again approximately a $\pi/2$ phase lag in the fluid response. The maximum velocity in the core region during a cycle is about 50 mm s^{-1}. The thickness of the acoustic boundary layer is in the range of 70–80 µm.

(ii) Second natural mode: The instantaneous velocity profiles obtained from PIV measurements for the second natural mode are shown in figure 14 for times $t/T =$ 0.10, 0.21, 0.32,0.37, 0.53, 0.65, 0.77, 0.87, and 0.96 ($T = 429$ µs). The maximum velocity in the core region during a cycle is about 100 mm s^{-1} and the thickness of the acoustic boundary layer is about 40–50 µm.

(iii) Third natural mode: The instantaneous velocity profiles obtained from PIV measurements for the third natural mode are shown in figure 15 for times $t/T = 0.05$, 0.20, 0.39, 0.55, 0.74, and 0.91($T = 263$ µs). The maximum velocity in the core region during a cycle is about 150 mm s^{-1} and the thickness of the acoustic boundary layer is about 30–40 µm.

3.4. *Comparison between theory and data*

3.4.1. *Standing wave theory*

Consider a tube of cross-sectional dimension d, filled with a liquid with density ρ and speed of sound c, driven at $x = 0$ such that the particle velocity is $u(0, t) = u_o \cos \omega t$ and terminated at $x = L$ such that $p(L, t) = 0$ (figure 1). The characteristic wavelength $\lambda \gg d$ for the operating frequency range and it is further assumed that the tube wall is rigid.

Under these conditions, the pressure wave propagates along the tube according to the following one-dimensional wave equation:

$$\frac{\partial^2 p}{\partial t^2} = c^2 \frac{\partial^2 p}{\partial x^2} \tag{3.1}$$

By applying the boundary conditions at $x = 0$ and $x = L$ and using $u(x, t) = -(1/\rho) \int \partial p/\partial x \mathrm{d}t$, the acoustic pressure in the tube is

$$p(x, t) = -\rho c u_o \frac{\sin[k(L - x)] \sin \omega t}{\cos kL}, \tag{3.2}$$

where $k = \omega/c$.

Similarly, the particle velocity is

$$u(x, t) = u_o \frac{\cos[k(L - x)] \cos \omega t}{\cos kL}. \tag{3.3}$$

As mentioned in § 2.1, the above assumption on the rigidity of the tube wall is not true and the effect of elasticity of the wall material should be considered. For example, in an air-filled tube, the impedance difference between the Pyrex wall and air is sufficient to render the tube wall effectively rigid. In a liquid-filled tube, however, the difference in impedance between the Pyrex wall and liquid is not nearly as great. A liquid-filled tube is in essence an elastic waveguide that can support a higher-order mode at all frequencies. The problem can be simplified by adopting the above rigid waveguide equations, but with a modified effective speed of sound accounting for the tube wall elasticity and acoustic coupling to the compliant wall, since the waves travelling within the tube are still nearly planar and the expected deviation from planar behaviour very small. A higher-order mode may exist at all frequencies, but it is not effectively excited by the piezo disk oscillating in this relatively lower-frequency range containing the first few longitudinal standing wave modes. Hence, this mode would be expected to possess very low amplitude. Note that as the liquid column is displaced back and forth, the interface that is held by surface tension recedes and advances, acting as a nonlinear spring. This may influence the fluid dynamics when the liquid column is short. This effect is neglected since the force due to surface tension is two orders of magnitude smaller than the inertial force of the liquid column, even when driven at the first natural frequency mode.

The acoustic pressure becomes unbounded when $\cos kL = 0$ in equation (3.3). Therefore, the natural frequencies for the driven/pressure release tube are

$$f_n = \frac{c}{2L}(n + 1/2), n = 0, 1, 2, 3, \ldots . \tag{3.4}$$

From the above relation (3.4) and the observed natural frequencies, the effective speed of sound can be estimated to be 856, 963, and $942\,\mathrm{m\,s^{-1}}$ for the first, second, and third natural frequency, respectively.

By using these numbers for the effective speed of sound and integrating equation (3.3) for the particle velocity $u(x, t)$ over time, the displacement amplitude (DA) along the tube can be obtained by

$$DA = 2\left|\int_0^{T/4} u_o \frac{\cos[k(L-x)]\cos\omega t}{\cos kL}\mathrm{d}t\right| = \left|\frac{u_o}{\pi f}\frac{\cos[k(L-x)]}{\cos kL}\right|. \tag{3.5}$$

In the above solution for the displacement amplitude along the tube, the factor u_o is still unknown as it is highly dependent on the physical mounting condition of the piezo disk (e.g. the amount of epoxy used, the glued area along the perimeter of the piezo disk, etc.). In addition, the damping effect is neglected in equation (3.1). Hence, rather than comparing the absolute displacement amplitudes, the above equation is normalized by the maximum value of the displacement amplitude ($DA_{\max}$) at the antinode at $x = L$:

$$DA_{\max} = \left|\frac{u_o}{\pi f \cos kL}\right|, \tag{3.6}$$

$$DA* = \frac{DA}{DA_{\max}} = |\cos[k(L-x)]|. \tag{3.7}$$

Figure 8 compares the normalized displacement amplitude, $DA*$, predicted from the analytical solution to the experimental data. The agreement is good for the second and third natural modes but figure 8(*a*) corresponding to the first natural mode exhibits certain deviation near the nodal point. The reason for this deviation in the case of the first natural mode has already been explained in § 3.1.

3.4.2. *The timing of fluid response*

Figure 16 shows the variation of normalized fluid velocity in the core region as time varies during a cycle. All experimental data points (solid squares in figure 16) are located near the fitted sinusoidal curve (centred line in figure 16) and the variation of fluid velocity seems to follow a harmonic function as can be expected from standing

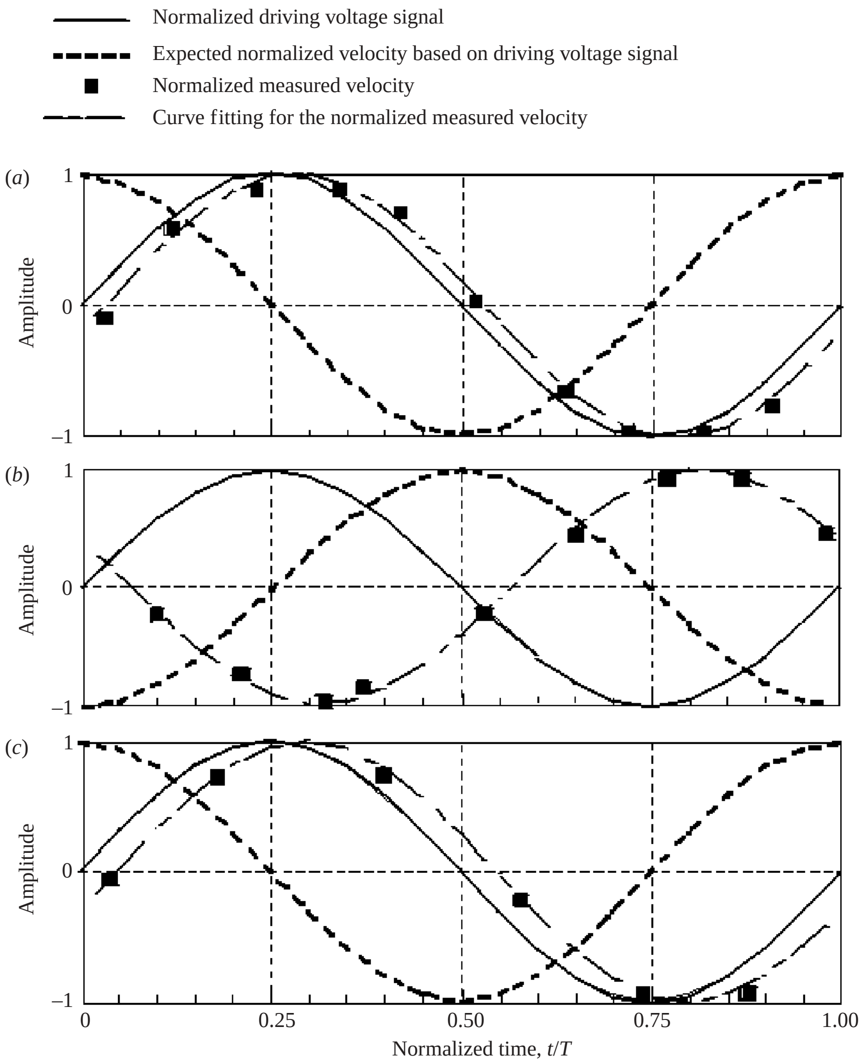

FIGURE 16. The response of fluid flow relative to the driving sinusoidal signal (water). (*a*) The first natural mode, (*b*) the second natural mode, (*c*) the third natural mode.

wave theory. In the figure, the solid line represents the sinusoidal voltage signal supplied to the piezo disk, which is in phase with the displacement of the piezo disk assuming that the loss and/or absorption in the piezo material is negligible. The phase of the piezo disk velocity leads that of the piezo disk displacement by $\pi/2$. From this, the phase of the fluid velocity at 2 cm from the open end can be obtained as the bold dotted line. For all modes, the measured fluid velocity has a phase lag slightly larger than $\pi/2$, which is due to the inherent phase delay between the driving sinusoidal voltage signal and the actuation of the piezo disk.

3.4.3. *The velocity in the acoustic boundary layer near the wall*

For simplicity, the x-direction will be taken in the direction of the flow along the tube wall surface, and the y-direction will be normal to the surface. In the acoustic boundary layer near the wall, the fluid medium can be considered as infinite in the y-direction. A simple, two-dimensional model can be established since the total cross-sectional dimension of the tube $d = 3000\,\mu\mathrm{m}$ and the acoustic boundary layer thickness is on the order of several tens of microns. For two-dimensional, unsteady, compressible, and Newtonian flow with only one velocity component in the x-direction, the Navier–Stokes equation is reduced to

$$\rho\frac{\partial u}{\partial t} + \frac{\partial p}{\partial x} = (2\mu + \lambda)\frac{\partial^2 u}{\partial x^2} + \mu\frac{\partial^2 u}{\partial y^2}, \tag{3.8}$$

where μ is dynamic viscosity of liquid and λ is bulk viscosity of liquid. For the same conditions, the continuity equation can also be written

$$\frac{1}{\rho c^2}\frac{\partial p}{\partial t} + \frac{\partial u}{\partial x} = 0. \tag{3.9}$$

The boundary conditions are

$$\left.\begin{array}{l} u(x, y, t) = 0 \quad \text{at} \quad y = 0\,(\text{no slip at the wall}), \\ u(x, y, t) \rightarrow u_\infty(x, t) \quad \text{as} \quad y \rightarrow \infty. \end{array}\right\} \tag{3.10}$$

In the above boundary conditions, the instantaneous core fluid velocity $u_\infty(x, t)$ is already known from the standing wave solution (equation (3.3)):

$$u_\infty(x, t) = u(x, t) = u_o\frac{\cos[k(L - x)]\cos\omega t}{\cos kL}. \tag{3.11}$$

These governing equations and boundary conditions have been solved numerically and figures 13, 14, 15 show the comparison between theory and experiment for the first, second, and third natural modes, respectively. Again, since u_o is still unknown, the velocity u was normalized by the maximum velocity 2 cm from the open end. It is noted that particles in the vicinity of a wall may interact with the solid boundary, so they can lag the fluid more than in an unbounded domain (Kim & Karrila 1991). This could be one of the reasons for the observed deviation between experiment and theory.

4. Glycerol–water mixture experiments: the effect of viscosity

The same experiment described in detail in the preceding section was carried out with a different fluid to investigate the effect of viscosity on the propagation of pressure waves in the standing wave tube and the overall flow structure. A glycerol–water mixture (50 %–50 % by volume) whose viscosity (∼6.1 cP) is higher than that of water by six times at room temperature was used as a working fluid.

The overall shape of the standing waves in the glycerol–water mixture shown in figure 17 was almost the same as with water. The first natural mode was observed at 670 Hz which is slightly lower than that for the water-filled case (690 Hz), while the second and third natural modes were observed at 2330 Hz and 3800 Hz, respectively, which were almost the same as in the water-filled case. For all three modes, the positions of the nodal points and antinodes were the same as in the water-filled case. The maximum displacement amplitude of 26 μm at the antinode is about the same as for the water case for the first natural mode and somewhat smaller for second and third natural modes at 14–15 μm for both. The agreement between the calculation and the experiment is good for the second and third natural modes, while some deviation is observed near the nodal point for the first mode. This deviation becomes greater

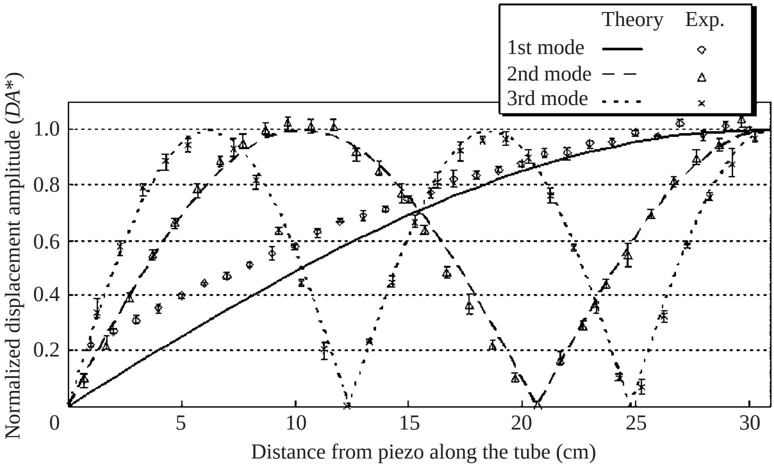

FIGURE 17. Normalized displacement amplitude, DA^* ($=DA/DA_{max}$) at the first three natural modes of standing wave inside the tube filled with glycerol–water mixture (50 %–50 %). The first natural mode was observed at 670 Hz and DA_{max} was 26 μm. The second natural mode and the third one were observed at 2330 Hz and 3800 Hz, respectively and DA_{max} was 14–15 μm.

approaching the nodal point and can be explained by the longer wavelength of the first natural mode as in § 3.1.

From the observed natural frequencies for the first three modes, the effective speed of sound (or phase velocity) can be estimated to be 831 m s^{-1}, 963 m s^{-1}, and 942 m s^{-1}, respectively. Even though the speed of sound is greater in the glycerol–water mixture than in water, the observed phase velocity is almost the same in the two cases. The reason for this is that 'the elastic waveguide effect' is also greater in this mixture case and tends to decrease the phase velocity through the standing wave tube since the acoustic impedance difference between the Pyrex wall and the glycerol–water mixture is smaller than that between the Pyrex wall and the water medium.

The bandwidth measurement results (displacement amplitude and FWHM) were nearly the same as for the water-filled tube. Even though the overall shape of standing waves and their bandwidth characteristics were almost the same as in the water-filled tube, the flow structure near the wall exhibited some differences. As figures 18, 19, and 20 show, the normalized velocity profile is nearly flat in the core region of the tube, but the acoustic boundary layer is now much thicker.

The increase in the thickness of the acoustic boundary layer stems from the higher viscosity since the acoustic boundary layer thickness δ is proportional to the square root of viscosity as follows:

$$\delta \sim \sqrt{\frac{\mu}{\rho\omega}}. \tag{4.1}$$

Even though the boundary layer thickness is inversely proportional to the square root of fluid density, the density increase is not great. Taking the higher viscosity of the glycerol–water mixture to be about six times that of water and a slight increase in fluid density, the thickness of acoustic boundary layer should be greater than the water-filled case by a factor of about 2.3. Experimental results in figures 18, 19, and 20 are in good agreement with this reasoning. The thickness of the acoustic boundary layer is about 160–180 μm for the first natural mode and less for the second and third natural modes. Therefore, it is still acceptable to have the two-dimensional

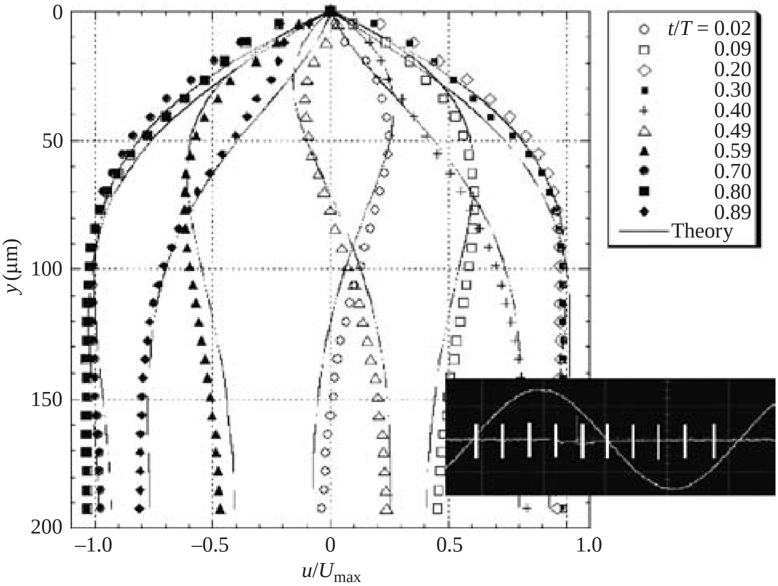

FIGURE 18. The comparison of normalized velocity profile variation for the first natural mode between theory and experiment (glycerol–water mixture). Each velocity profile corresponds to the temporal location marked as a white bar in the sinusoidal voltage signal that is supplied to the piezo disk.

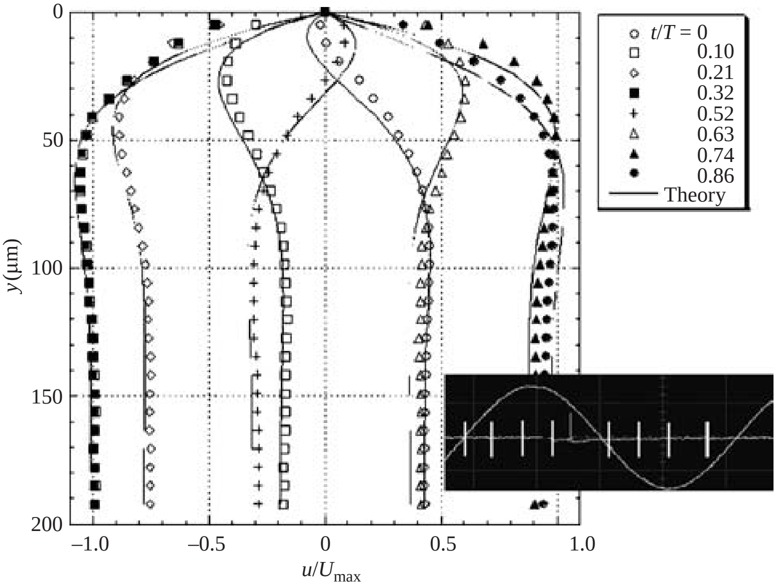

FIGURE 19. As figure 18 but for the second natural mode.

measurement (or focal) plane located about 200 μm below the top wall/liquid interface since this measurement plane will remain outside the acoustic boundary layer for all three cases.

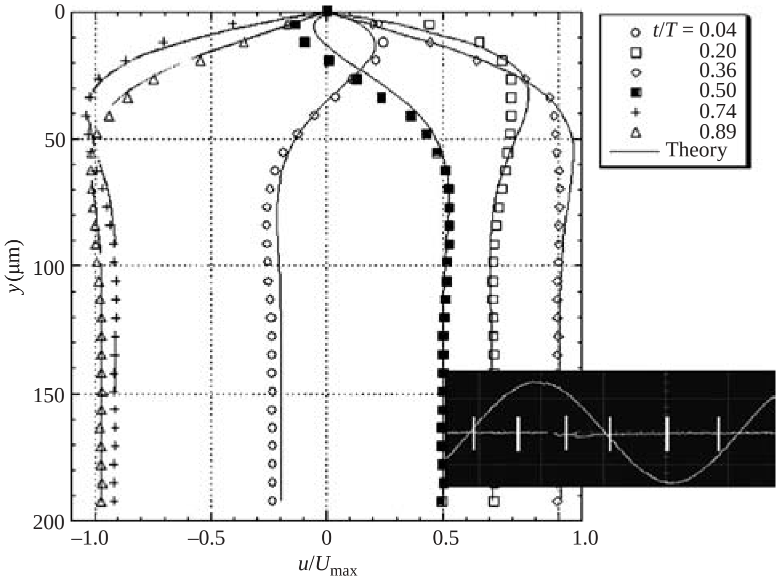

FIGURE 20. As figure 18 but for the third natural mode.

(i) First natural mode (figure 18): the instantaneous velocity vector fields resulting from PIV measurements for the first natural mode were acquired for times $t/T = 0.02$, 0.09, 0.20, 0.30, 0.40, 0.49, 0.59, 0.70, 0.80, and 0.89 ($T = 1493$ μs). The maximum velocity in the core region during a cycle is about 50 mm s^{-1} and the acoustic boundary layer thickness can be estimated to be about 160–180 μm, which is approximately 2.3 times that of the water-filled tube in the first natural mode.

(ii) Second natural mode (figure 19): the instantaneous velocity vector fields for the second natural mode were acquired for times $t/T = 0$, 0.10, 0.21, 0.32, 0.52, 0.63, 0.74, and 0.86 ($T = 429$ μs). The maximum velocity in the core region during a cycle is about 95 mm s^{-1} and the thickness of acoustic boundary layer is estimated to be about 90–110 μm.

(iii) Third natural mode (figure 20): the instantaneous velocity vector fields for the third natural mode were acquired for times $t/T = 0.04$, 0.20, 0.36, 0.50, 0.74, and 0.89 ($T = 263$ μs). The maximum velocity in the core region during a cycle is about 145 mm s^{1} and the thickness of the acoustic boundary layer is about 70–90 μm.

The calculated normalized velocity profiles were obtained from the governing equation (3.8) and boundary conditions (3.10) using a different constant viscosity (∼6.1 cP). Typically, each experimental run was performed over a period of 10 hours. Temperature variation of several degrees may arise during this period. Consequently, the viscosity can change; the viscosity of glycerol–water mixture changes by about 15 % per 5 °C ambient temperature difference, compared to 9 % for water. This would result in relatively larger deviation between experimental measurements and theoretical prediction for the glycerol–water mixture case.

Figure 21 shows the variation of fluid velocity in the core region during a cycle. The results are nearly the same as the case of the water-filled tube.

5. Conclusion

The liquid flow structure inside a standing wave tube was measured using the PIV technique while operating the standing wave tube at natural frequencies. The

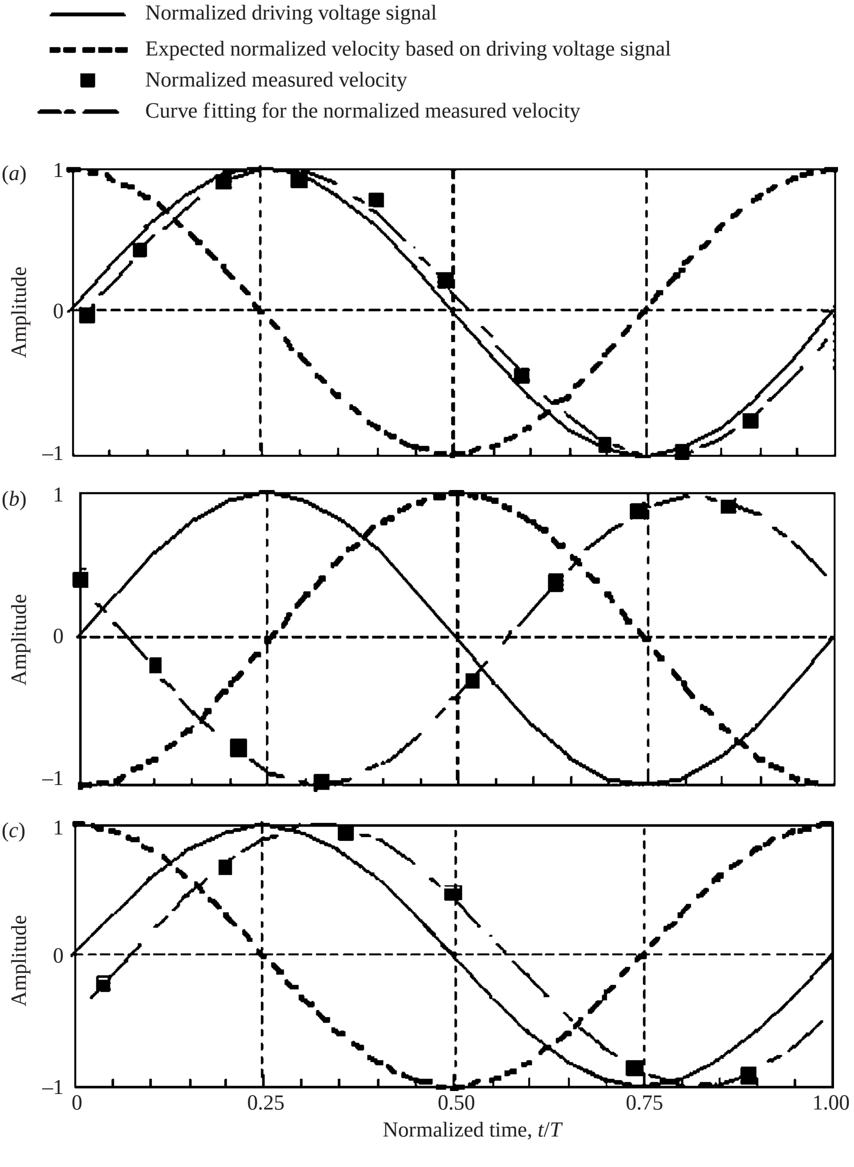

FIGURE 21. The response of fluid flow relative to the driving sinusoidal signal (glycerol–water mixture). (*a*) The first natural mode, (*b*) the second natural mode, (*c*) the third natural mode.

driving frequency was in the range from several hundred Hz to several kHz. The wavelength corresponding to this range of driving frequency is much greater than the cross-sectional dimension (3 mm) of the tube and is comparable to the total length of the tube. The nature of wave propagation through the standing wave tube is nearly one-dimensional under these conditions. Therefore, once the piezo disk is actuated at the natural frequency, the liquid inside the tube responds as an elastic solid bar driven at one end and free at the other end. The fluid particles undergo periodic compression and expansion according to the driving frequency. The velocity profile is nearly flat across the tube except in a very thin region near the wall. Since the fluid has to satisfy the no-slip condition at the wall, an acoustic boundary layer develops.

The overall shape of the standing waves was visualized for the first three natural modes. The first, second, and third natural modes were formed in water at 690 Hz, 2.33 kHz, and 3.8 kHz respectively. The bandwidth was also measured and the FWHM was about 200 Hz for the first and third modes and ∼250 Hz for the second mode. PIV images were taken and processed to acquire the velocity vector field, at several different temporal locations during a cycle. The experimental results showed that the acoustic boundary layer thickness was reduced with increasing frequency and in any case was less than 100 μm. The overall shape measured and PIV results including the observed flow reversal show very good agreement with theory.

The same set of experiments was carried out with a glycerol–water mixture to examine the effect of viscosity. The overall shape and bandwidth characteristics were almost the same as in the case of a water-filled tube. In contrast, due to the higher viscosity, the acoustic boundary layer thickness was larger by a factor of 2.3. These experimental results also compared very well with theory.

This work was supported by a Xerox Corp. grant to the Laser Thermal Laboratory of UC Berkeley.

REFERENCES

Adrian, R. J. 1991 Particle-imaging techniques for experimental fluid mechanics. *Annu. Rev. Fluid Mech.* **23**, 261–304.

Hann, D. B. & Greated, C. A. 1997*a* Measurement of acoustic particle velocity using particle image velocimetry techniques. *Acoustica* **83**, 354–358.

Hann, D. B. & Greated, C. A. 1997*b* Particle image velocimetry for the measurement of mean and acoustic particle velocities. *Meas. Sci. Technol.* **8**, 656–660.

Hann, D. B. & Greated, C. A. 1997*c* The measurement of flow velocity and acoustic particle velocity using particle-image velocimetry. *Meas. Sci. Technol.* **8**, 1517–1522.

Hjelmfelt, A. T. & Mockros, L. F. 1966 Motion of discrete particles in a turbulent fluid. *Appl. Sci. Res.* **16**, 149–161.

Kim, S. & Karrila, S. J. 1991 *Microhydrodynamics: Principles and Selected Applications.* Butterworth-Heinemann.

Lafleur, L. D. & Shields, F. D. 1995 Low-frequency propagation modes in a liquid-filled elastic tube Waveguide. *J. Acoust. Soc. Am.* **97**, 1435–1445.

Meinhart, C. D., Wereley, S.T. & Gray, M. H. B. 2000 Volume illumination for two-dimensional particle image velocimetry. *Meas. Sci. Technol.* **11**, 809–914.

Meinhart, C. D., Wereley, S. T. & Santiago, J. G. 1999 PIV measurements of a microchannel flow. *Exps. Fluids* **27**, 414–419.

Melling, A. 1997 Tracer particles and seeding for particle image velocimetry. *Meas. Sci. Technol.* **8**, 1406–1416.

Santiago, J. G., Wereley, S. T., Meinhart, C. D., Beebe, D. J. & Adrian, R. J. 1998 A micro particle image velocimetry system. *Exps. Fluids* **25**, 316–319.

Vignola, J. F., Berthelot, Y. H. & Jarzynski, J. 1990 Laser detection of sound. *J. Acoust. Soc. Am.* **90**, 1275–1286.

Wilson, P. S. 2002 Sound propagation and scattering in bubbly liquids. PhD dissertation. Boston University.